

Accepted for publication in *Ap.J.* 1999 February 20

ORFEUS II and IUE Spectroscopy of EX Hydrae

Christopher W. Mauche¹

Lawrence Livermore National Laboratory,
L-43, 7000 East Avenue, Livermore, CA 94550;
mauche@cygnus.llnl.gov

¹*ORFEUS-SPAS II* Guest Investigator

ABSTRACT

Using five high-resolution ($\lambda/\Delta\lambda \approx 3000$) FUV ($\lambda\lambda = 910\text{--}1210 \text{ \AA}$) spectra acquired in 1996 December during the flight of the *ORFEUS-SPAS II* mission, 47 archival *IUE* short-wavelength UV ($\lambda\lambda = 1150\text{--}1950 \text{ \AA}$) spectra, and archival *EUVE* deep survey photometry ($\lambda\lambda \approx 70\text{--}200 \text{ \AA}$), we present a detailed picture of the behavior of the magnetic cataclysmic variable EX Hydrae in the vacuum ultraviolet. Like *HUT* spectra of this source, these FUV and UV spectra reveal broad emission lines of He II, C II–IV, N III and V, O VI, Si III–IV, and Al III superposed on a continuum which is blue in the UV and nearly flat in the FUV. Like *ORFEUS* spectra of AM Her, the O VI $\lambda\lambda 1032, 1038$ doublet is resolved into broad (FWHM $\approx 2000 \text{ km s}^{-1}$) and narrow (FWHM $\approx 200 \text{ km s}^{-1}$) emission components. Consistent with its behavior in the optical, and hence consistent with the accretion curtain model of this source, the FUV and UV continuum flux densities, the FUV and UV broad emission line fluxes, and the radial velocity of the O VI broad emission component all vary on the spin phase of the white dwarf, with the maximum of the FUV and UV continuum and broad emission line flux light curves coincident with maximum *blueshift* of the broad O VI emission component. On the binary phase, the strong eclipse of the EUV flux by the bulge on the edge of the accretion disk is accompanied by narrow and relatively weak absorption components of the FUV emission lines and 30%–40% eclipses of all the UV emission lines except He II $\lambda 1640$, while the UV continuum is largely unaffected. Furthermore, both the flux and radial velocity of the O VI narrow emission component vary with binary phase. The relative phasing of the FUV and UV continuum light curves and the FUV emission-line radial velocities implicate the accretion funnel as the source of the FUV and UV continuum and the O VI broad emission component, and the white dwarf as the source of the O VI narrow emission component. Various lines of evidence imply that the density of both the broad- and narrow-line regions is $n \gtrsim 10^{11} \text{ cm}^{-3}$, but the O VI line ratios imply that the narrow-line region is optically thick while the broad-line region is more likely optically thin.

Subject headings: binaries: close — stars: individual (EX Hydrae) — stars: magnetic fields — ultraviolet: stars — white dwarfs

1. Introduction

Among the classes of cataclysmic variables (CVs), there is one in which the magnetic field of the white dwarf is strong enough to influence the flow of material lost by the secondary. These magnetic CVs are subdivided into the spin-synchronous ($P_{\text{spin}} \approx P_{\text{orb}}$) polars (AM Her stars) and the spin-asynchronous ($P_{\text{spin}} < P_{\text{orb}}$) intermediate polars (DQ Her stars). In polars, the accreting matter is channeled along the magnetic field lines for most of its trajectory from the secondary’s inner Lagrange point to the white dwarf surface, while in intermediate polars (IPs), accretion is moderated by a disk. Although the disk maintains an essentially Keplerian velocity profile at large radii, it is truncated at small radii where the magnetic stresses become large enough to remove the disk angular momentum in a radial distance which is small compared to the distance to the white dwarf; the material then leaves the disk and follows the magnetic field lines down to the white dwarf surface in a manner similar to that of polars. In either class of magnetic CVs, the velocity of the flow as it nears the white dwarf is highly supersonic [$v = 3600 (M_{\text{wd}}/0.5 M_{\odot})^{1/2} (R_{\text{wd}}/10^9 \text{ cm})^{-1/2} \text{ km s}^{-1}$], hence to match boundary conditions, the flow must pass through a strong shock far enough above the white dwarf surface for the hot [$kT = 16 (M_{\text{wd}}/0.5 M_{\odot}) (R_{\text{wd}}/10^9 \text{ cm})^{-1} \text{ keV}$], post-shock flow to be decelerated by pressure forces and settle on the white dwarf surface. Magnetic CVs are therefore strong X-ray sources modulated at the spin period of the white dwarf. For additional details of magnetic CVs, see Cropper (1990), Patterson (1994), and Warner (1995); for recent results, see the volumes by Buckley & Warner (1995) and Hellier & Mukai (1999).

EX Hydrae is a bright ($V \approx 13$), high-inclination ($i = 77^\circ \pm 1^\circ$), eclipsing IP with an orbital period of 98.26 minutes and a white dwarf spin period of 67.03 minutes. The mass of the white dwarf is measured by both dynamical (Hellier 1996) and X-ray spectroscopic (Fujimoto & Ishida 1997) methods to be $M_{\text{wd}} = 0.49 M_{\odot}$, while details of the accretion geometry are established by the optical and X-ray observations of Hellier et al. (1987) and Rosen, Mason, & Córdoba (1988). In the resulting “accretion curtain” model of EX Hya specifically and IPs in general, the spin-phase modulations are the result of the angular offset between the spin and magnetic dipole pole axes and the consequent strong azimuthal asymmetry of the flow of material from the disk to the surface of the white dwarf. Because of absorption by this accretion curtain, the spin-phase light curves peak when the upper pole points *away* from the observer—when the blueshift of the emission lines is maximum. In addition to this spin-phase modulation, binary-phase modulations are produced by partial eclipses by the secondary and by the bulge on the edge of the accretion disk.

EX Hya has been studied extensively in the X-ray and optical wavebands (in addition to the references above, see, e.g., Siegel et al. 1989; Rosen et al. 1991; Allan, Hellier, & Beardmore 1998; Mukai et al. 1998), but less so at UV and FUV wavelengths. Despite the 174 *International Ultraviolet Explorer* (IUE) spectra of EX Hya in the archive, the discussion of these UV data has been limited to the papers by Bath, Pringle, & Whelan (1980, written before EX Hya was recognized as an IP), Krautter & Buchholz (1990, a 2-page paper in a conference proceedings),

and the statistical studies of Verbunt (1987), la Dous (1991), and Mauche, Lee, & Kallman (1997). Greeley et al. (1997) recently described and modeled UV–FUV spectra of this source acquired with the *Hopkins Ultraviolet Telescope (HUT)* during the Astro-2 mission in 1995 March. To extend the effort of documenting the phenomenology and understanding the accretion geometry of EX Hya, we here analyze and discuss five FUV spectra of this source acquired in 1996 December during the flight of the *Orbiting and Retrievable Far and Extreme Ultraviolet Spectrograph–Shuttle Pallet Satellite (ORFEUS-SPAS) II* mission. These spectra are superior those of *HUT* because of the higher spectral resolution and more extensive phase coverage, but suffer from the narrower bandpass. To help offset this shortcoming, we make use of an extensive set of *IUE* spectra of EX Hya obtained in 1995 June by K. Mukai. For completeness and ease of reference, we also present and describe the EUV/soft X-ray spin- and binary-phase light curves of EX Hya measured by *EUVE* in 1994 May–June (Hurwitz et al. 1997). AAVSO measurements during and near the times of these observations demonstrate that in each instance EX Hya was at its quiescent optical magnitude of $V \approx 13$ (Mattei 1998).

2. EUVE Photometry

As described in detail by Hurwitz et al. (1997), EX Hya was observed by *EUVE* for 150 kiloseconds beginning on 1994 May 26.² The resulting deep survey ($\lambda \approx 70\text{--}200$ Å) spin- and binary-phase count rate light curves are shown in Figure 1, where the ephemerides of Hellier & Sproats (1992) have been employed to convert HJD photon arrival times to white dwarf spin and binary phases.³ Due to the $\sim 30\%$ efficiency of *EUVE* observations, the photons from whence these light curves were constructed were acquired over an interval of 6.5 days (from HJD 2449498.89420 until 2449505.42824). This observation was therefore sufficiently long to avoid the spin- and binary-period aliasing typical of low-Earth-orbit satellite observations of EX Hya, including the *ORFEUS* and *IUE* observations described below.

The binary-phase *EUVE* light curve of EX Hya is shown in the middle and lower panels of Figure 1 and is seen to manifest a broad dip at $\phi_{98} \approx 0.85^{+0.15}_{-0.25}$ and a narrow eclipse at $\phi_{98} \approx 0.97$. The dip is understood to be due to the passage through the line of sight of the bulge on the edge of the accretion disk caused by the impact of the accretion stream. With a residual intensity of approximately 0.13, the optical depth of the bulge is $\tau \approx 2.0$ at $\lambda \approx 90$ Å, the peak of the effective area curve of the deep survey instrument. If the occulting material is neutral and has

²For the record, note that Hurwitz et al. (1997) erroneously report that the *EUVE* observation of EX Hya began on 1994 May 29; this date is actually the midpoint of the observation. Similarly, the dates referred to in §2.1 (§2.3) of that paper are not the first, but the ≈ 48 th (≈ 70 th) observed binary eclipse (spin maximum).

³The sinusoidal term in the binary ephemeris of Hellier & Sproats (1992) is ignored here and elsewhere in this paper because it is uncertain and because it has a full range of only 48 seconds or 0.008 binary cycles; at the midpoint of the *EUVE* observation, the correction amounts to -41 seconds or -0.007 binary cycles.

solar abundances (specifically, one He atom for every ten H atoms), the inferred column density is $N_{\text{H}} \approx 7.4 \times 10^{19} \text{ cm}^{-2}$. Such a column is essentially transparent ($\tau \leq 0.01$) above 1.2 keV, consistent with the fact that the dip is seen only in soft X-rays (e.g., Rosen, Mason, & Córdova 1988). The narrow eclipse is understood to be due to the grazing occultation of the EUV/soft X-ray emission region by the secondary. Fitting a linear background minus a Gaussian to the interval $\phi_{98} = 0.95\text{--}0.99$, we find that the eclipse is centered at $\phi_{98} = 0.9714 \pm 0.0003$, has a FWHM = 0.007 ± 0.001 or 38 ± 6 seconds, and a full width of $\Delta\phi_{98} \sim 0.01$ or 60 seconds; the residual intensity at mid-eclipse is consistent with zero at $0.014 \pm 0.013 \text{ counts s}^{-1}$. In contrast, the eclipse by the secondary of the hard X-ray emission region is significantly wider ($\Delta\phi_{98} \approx 0.03$ or 180 seconds) and partial (eclipse depth = 30–60%; Beuermann & Osborne 1988; Rosen et al. 1991; Mukai et al. 1998). The centroid of the hard X-ray eclipse was recently measured with *RXTE* by Mukai et al. (1998) to be centered at $\phi_{98} = 0.98$, reinforcing the impression that the binary ephemeris of Hellier & Sproats (1992) may need to be updated.

The spin-phase *EUVE* light curve of EX Hya is shown in the upper panel of Figure 1 and is seen to vary more sharply than a sine wave, but it is nonetheless reasonably well approximated by the sinusoidal function $A + B \sin 2\pi(\phi_{67} - \phi_0)$ with $A = 0.158 \pm 0.001 \text{ counts s}^{-1}$, $B = 0.105 \pm 0.002 \text{ counts s}^{-1}$, and $\phi_0 = 0.790 \pm 0.002$. The relative pulse amplitude is therefore $B/A = 67\% \pm 1\%$ and the light curve peaks at $\phi_{67} = 0.040 \pm 0.002$. This phasing again is formally different from the ephemeris of Hellier & Sproats (1992), but it establishes to sufficient accuracy for the present purposes that the EUV/soft X-ray light curve peaks at $\phi_{67} \approx 0$.

3. ORFEUS Spectroscopy

The FUV spectra of EX Hya were acquired with the Berkeley spectrograph in the *ORFEUS* telescope during the flight of the *ORFEUS-SPAS II* mission in 1996 November–December. The general design of the spectrograph is discussed by Hurwitz & Bowyer (1986, 1996), while calibration and performance of the *ORFEUS-SPAS II* mission are described by Hurwitz et al. (1998); for the present purposes, it is sufficient to note that the spectra cover the range $\lambda\lambda = 910\text{--}1210 \text{ \AA}$ and that the mean instrument profile FWHM $\approx 0.33 \text{ \AA}$, hence $\lambda/\Delta\lambda \approx 3000$. Acquisition of the *ORFEUS* exposures was complicated by the fact that the satellite period (91 min) nearly equals the binary orbital period and four thirds of the white dwarf spin period. After consulting with B. Greeley it was decided to concentrate on the spin period, with observations every satellite orbit for 6 orbits, but practical considerations resulted in the coverage shown in Figure 1 and detailed in Table 1, which lists the HJD of the start of the exposures, the length of the exposures, and the range of binary and spin phases assuming the ephemerides of Hellier & Sproats (1992).

Figure 2 shows the background-subtracted and flux-calibrated *ORFEUS* spectra binned to a resolution of 0.1 \AA and smoothed with a 5-point triangular filter. Relatively strong residual geocoronal emission lines of H I $\lambda 1025.7$ (Lyman β), He I $\lambda 584.3$ (at 1168.7 \AA in second order), N I $\lambda 1134$, $\lambda 1200$, and O I $\lambda 988.7$ have been subtracted from these spectra by fitting Gaussians in

the neighborhood ($\pm 5 \text{ \AA}$) of each line. The remaining geocoronal emission lines are all very weak and contaminate only a limited number of discrete ($\text{FWHM} \approx 0.8 \text{ \AA}$) portions of the spectra. These FUV spectra are generally consistent with the *HUT* spectra acquired 1995 March (Greeley et al. 1997), with emission lines of O VI $\lambda\lambda 1032, 1038$ and C III $\lambda 977, \lambda 1176$ superposed on a nearly flat continuum. The broad and variable emission feature at $\lambda \approx 990 \text{ \AA}$ is likely N III, but the flux and position of this feature are uncertain because it coincides with a strong increase in the background at $\lambda \approx 1000 \text{ \AA}$ which renders noisy the short-wavelength end of these spectra.

To quantify the continuum flux density variations of the FUV spectra of EX Hya, we measured the mean flux density at $\lambda = 1010 \pm 5 \text{ \AA}$. This choice for the continuum bandpass is somewhat arbitrary, but it avoids the noisy portion of the spectra shortward of $\lambda \approx 1000 \text{ \AA}$ and the broad weak bump between the O VI and C III $\lambda 1176$ emission lines. Ordered by spin phase, the mean flux density in this bandpass is $f_{1010}(10^{-12} \text{ erg cm}^{-2} \text{ s}^{-1} \text{ \AA}^{-1}) = 0.181, 0.163, 0.130, 0.171, \text{ and } 0.236$. Of the spin and binary phases, it appears that these flux density variations occur on the spin phase, since as shown in Figure 3 they are reasonably well fitted ($\chi^2/\text{dof} = 6.4/2$ assuming 5% errors in the flux densities) by $f_{1010}(10^{-12} \text{ erg cm}^{-2} \text{ s}^{-1} \text{ \AA}^{-1}) = A + B \sin 2\pi(\phi_{67} - \phi_0)$ with $A = 0.192 \pm 0.005$, $B = 0.049 \pm 0.007$, and $\phi_0 = 0.743 \pm 0.023$; on the binary phase, the fit is significantly poorer ($\chi^2/\text{dof} = 28.8/2$). The relative FUV continuum pulse amplitude is therefore $B/A = 25\% \pm 4\%$ and the light curve peaks at $\phi_{67} = -0.01 \pm 0.02 \approx 0$, consistent with the EUV/soft X-ray light curve.

Since the *ORFEUS* bandpass is too narrow to meaningfully constrain the effective temperature, it is not possible to uniquely determine the cause of these continuum flux density variations: they could be due to variations in the effective temperature, variations in the effective size of the emission region, or some combination of these. Assuming $M_{\text{wd}} = 0.49 M_{\odot}$ ($R_{\text{wd}} = 9.8 \times 10^8 \text{ cm}$), $d = 100 \text{ pc}$, and that the entire white dwarf surface radiates with a blackbody spectrum, the effective temperature varies with phase according to $T_{\text{eff}}(\text{kK}) = 27.2 + 1.3 \sin 2\pi(\phi_{67} - 0.743)$. If, as for AM Her (Mauche & Raymond 1998), we instead assume that we are seeing a 20 kK white dwarf with 37 kK spot, the apparent projected area of the spot varies with binary phase according to $f = 0.058 + 0.018 \sin 2\pi(\phi - 0.743)$. To demonstrate that such two-temperature blackbody models do a good job of matching the *ORFEUS* spectra, we show in Figure 2 a series of 20 + 37 kK blackbody models superposed on the data.

Accompanying the continuum flux variations are variations in the flux and radial velocity of the emission lines. In what follows, we concentrate on the emission lines longward of $\lambda = 1000 \text{ \AA}$ where the spectra and hence the line fluxes and positions are not adversely affected by the high background and consequent low signal-to-noise ratio. Inspection of Figure 2 reveals that the spectra in the neighborhood of the C III $\lambda 1176$ emission line are sufficiently simple to allow fits with a linear continuum plus a Gaussian (5 free parameters), while the broad and narrow components of the O VI $\lambda\lambda 1032, 1038$ doublet require at a minimum a linear continuum plus four Gaussians. To constrain the fits of the O VI line, we constrain the separation of the doublets to their laboratory separation, and the widths of each component to be the same (for a total of 10

free parameters).

Figure 4 shows the success we have had with the fits of the O VI lines, with both the data and the models binned to a resolution of 0.1 \AA and smoothed with a 5-point triangular filter. Thanks to the high spectral resolution of the Berkeley spectrograph, the lines are cleanly resolved into narrow and broad components and it appears that the model produces reasonable fits of these complex line profiles. The most significant deviation of the fits relative to the data is in the last spectrum ($\phi_{67} = 0.767\text{--}1.152$ or $\phi_{98} = 0.663\text{--}0.926$), where the broad emission component of the doublet is cut by a pair of slightly blueshifted ($v < 300 \text{ km s}^{-1}$) narrow absorption features. A similar absorption component is present at that same phase in the C III emission lines, and it is likely not a coincidence that this absorption is strongest at the same binary phases where the EUV flux deficit is strongest ($\phi_{98} \approx 0.85 \pm 0.1$). For the present, it is sufficient to note that the presence of this absorption component does not appear to significantly affect the fits of the emission lines.

The fitting parameters for the broad and narrow components of the O VI emission line have been converted into physical quantities (flux, velocity, FWHM) and are listed in Table 2. The velocities of the broad and narrow components of the line were fit with a sinusoidal function of the form $v = \gamma + K \sin 2\pi(\phi - \phi_0)$, whereby it became apparent that the velocity of the broad component of the line varies with the spin phase while that of the narrow component varies with the binary phase. The parameters of these fits are shown in Table 3 and the data and the best-fit radial velocity curves are shown in Figure 5. Maximum blueshift of the broad component of the O VI line occurs at $\phi_{67} = 0.05 \pm 0.07 \approx 0$, while maximum blueshift of the narrow component of the line occurs at $\phi_{98} = 0.30 \pm 0.02 \sim 0.25$. As shown in Figure 6, these radial velocities anticorrelate nicely with the flux in the two components of the line. Specifically, the broad-line flux varies as $f_{\text{O VI, b}} (10^{-12} \text{ erg cm}^{-2} \text{ s}^{-1}) = A + B \sin 2\pi(\phi_{67} - \phi_0)$ with $A = 3.2 \pm 0.2$, $B = 1.8 \pm 0.2$, and $\phi_0 = 0.79 \pm 0.04$ (hence peaks at $\phi_{67} = 0.04 \pm 0.04 \approx 0$), while the narrow-line flux varies as $f_{\text{O VI, n}} (10^{-12} \text{ erg cm}^{-2} \text{ s}^{-1}) = C + D \sin 2\pi(\phi_{98} - \phi_0)$ with $C = 0.33 \pm 0.03$, $D = 0.12 \pm 0.03$, and $\phi_0 = 0.95 \pm 0.07$ (hence peaks at $\phi_{98} = 0.20 \pm 0.07 \approx 0.25$).

The behavior of the C III $\lambda 1176$ emission line is less straightforward. While the flux in the line clearly correlates with spin phase according to $f_{\text{C III}} (10^{-12} \text{ erg cm}^{-2} \text{ s}^{-1}) = E + F \sin 2\pi(\phi_{67} - \phi_0)$ with $E = 1.38 \pm 0.09$, $F = 0.75 \pm 0.10$, and $\phi_0 = 0.84 \pm 0.03$ (hence peaks at $\phi_{67} = 0.09 \pm 0.03 \sim 0$), the radial velocity ranges between $\pm 200 \text{ km s}^{-1}$ within the errors and can be fit satisfactorily on either the spin or binary phases with the parameters shown in Table 3. If the C III radial velocity varies with spin phase, it has maximum blueshift at $\phi_{67} = 0.26 \pm 0.08$; $\Delta\phi_{67} = 0.21 \pm 0.11$ *after* that of the O VI broad component, while if the C III radial velocity varies with binary phase, it has maximum blueshift at $\phi_{98} = 0.14 \pm 0.08$; $\Delta\phi_{98} = 0.15 \pm 0.09$ *before* that of the O VI narrow component. The former alternative is favored by the broad width of the line and the strong flux variation on the spin phase. However, because of the long exposures and the relatively poor phase coverage and because the line is broad and typically rather weak, it is not possible with the existing data to usefully constrain the phasing of the radial velocity variations of the C III $\lambda 1176$ emission line.

4. IUE Spectroscopy

As mentioned in the introduction, to date little has been done with the large number of *IUE* spectra of EX Hya in the archive. While a full analysis of these UV data is beyond the scope of the present work, it is nonetheless useful to perform an analysis of a subset of the existing spectra to extend the bandpass for which we have phase-resolved spectroscopic information for EX Hya. The 1995 March *HUT* spectra of EX Hya (Greeley et al. 1997) of course cover the UV and FUV wavebands simultaneously, but those observations are limited to some extent by the limited range of spin ($\phi_{67} = 0.05\text{--}0.50$) and binary phases ($\phi_{98} = 0.09\text{--}0.40$) sampled. Of the 174 *IUE* spectra in the archive, 124 are short-wavelength spectra ($\lambda\lambda = 1150\text{--}1950$ Å) obtained through the large aperture (i.e., are photometric). Of this subset, there is a continuous set of 45 spectra (SWP 55063–55107) with exposure times of 10 minutes obtained by K. Mukai over an interval of 1.3 days beginning on 1995 June 23. For the 41 spectra available from the *IUE* archive, Table 4 lists the sequence numbers, the HJD of the start of the exposures, and the range of binary and spin phases assuming the ephemerides of Hellier & Sproats (1992).

Unfortunately, even this extensive and continuous set of *IUE* spectra suffers from aliasing between the spin and binary periods. Specifically, the phases of the exposures in this sequence satisfy $\phi_{67} \approx (0.4 - \phi_{98}) \pm 0.2$. During the portion of the orbit unaffected by the dip ($\phi_{98} = 0.0\text{--}0.7$), there were 14 spectra obtained during spin maximum ($\phi_{67} = 0.8\text{--}1.2$), but only 7 spectra were obtained during spin minimum ($\phi_{67} = 0.3\text{--}0.7$); during the dip ($\phi_{98} = 0.75\text{--}0.95$), there were 6 spectra obtained during spin minimum, but none were obtained during spin maximum. To populate this portion of phase space, we extracted from the archive all (5) short-wavelength large-aperture spectra satisfying the constraint [$\phi_{98} = 0.75\text{--}0.95$, $\phi_{67} = 0.8\text{--}1.2$]. The relevant details of these spectra are included in Table 4.

From this subset of 32 *IUE* spectra of EX Hya, we produced the four mean phase-resolved spectra shown in Figure 7. From brightest to dimmest, the spectra were obtained during: (1) spin maximum away from the dip, (2) spin maximum during the dip, (3) spin minimum during the dip, and (4) spin minimum away from the dip. Like the *HUT* spectra, these spectra reveal emission lines of He II, C II–IV, N V, Si III–IV, and Al III superposed on a blue continuum. The most spectacular aspect of these spectra is the widths of the lines; the FWHM of the C IV line for instance is approximately 14 Å or 2700 km s^{−1} compared to 7–10 Å or 1400–1900 km s^{−1} for other magnetic CVs.

These mean spectra demonstrate the following effects on the UV lines and continuum as a function of spin and binary phase. First consider the effect of the dip. During spin maximum, the dip does not significantly affect the continuum or the He II line, but the flux in the other lines decreases by 30%–40%, with the red wings of the lines affected preferentially. During spin minimum, the continuum *increases* by roughly 20% during the dip, but there is little if any effect on the lines. Next consider variations on the spin phase. Away from the dip, the continuum decreases by roughly 40% going from spin maximum to spin minimum. The effect on the lines is

much more pronounced: the flux in the N V and Si IV lines decreases by roughly 60%, the flux in the C IV line decreases by roughly 80%, and the He II line disappears altogether. The lines also markedly change shape: the N V and Si IV lines become less centrally peaked, while the blue side of the C IV line is preferentially suppressed. During the dip, the continuum decreases by roughly 20% going from spin maximum to spin minimum, the flux in the C IV line decreases by roughly 60%, again with most of the action on the blue side of the line, and again the He II line disappears altogether.

To quantify the variations of the UV lines and continuum as a function of spin and binary phase, we attempted to fit the flux density of the individual spectra in the neighborhood of the C IV line ($\lambda = 1550 \pm 50$ Å) with a number of analytic functions. Ideally, the C IV line in these *IUE* spectra would be modeled the same way as O VI line in the *ORFEUS* spectra, with a linear continuum plus four Gaussians, but the *IUE* spectral resolution is insufficient to resolve the C IV line into its doublet components or to separately distinguish the emission and absorption components. The O VI narrow emission and absorption components are relatively weak, so there is some hope of successfully modeling the C IV line with a linear continuum plus one or two Gaussians (with 5 or 8 degrees of freedom, respectively). The simpler model faithfully measures the continuum flux density, but the overall fits are poor and the line parameters unreliable because a single Gaussian is incapable of reproducing the strongly asymmetric shape of the line during spin minimum. Good fits result if a second Gaussian (either in emission or absorption) is included in the model, but again the line parameters are unreliable because they tend to wander in their exploration of χ^2 space. After some experimenting, it was found that the most robust and reliable line parameters resulted using a model consisting of a linear continuum plus two Gaussians whose widths were fixed at 4.0 Å; specifically, $f_\lambda = f_1 + f_2\lambda' + f_3 \exp(-[\lambda' - \lambda_1]^2/2\sigma^2) + f_4 \exp(-[\lambda' + \lambda_2]^2/2\sigma^2)$, where $\sigma = 4.0$ Å, $\lambda' = \lambda - \lambda_0$, and $\lambda_0 = 1549.48$ Å, the optically thick mean of the laboratory wavelengths of the C IV doublet.

The spin-phase behavior of the resulting flux in the C IV emission line is shown in Figure 8 for binary phases during and away from the dip. In both cases, the C IV flux peaks at $\phi_{67} \approx 0$, but the amplitude and mean level of the oscillation is a strong function of binary phase. Excluding the anomalously low flux points shown by the diamonds, away from the dip the C IV flux varies as $f_{\text{C IV, out}} (10^{-12} \text{ erg cm}^{-2} \text{ s}^{-1}) = A + B \sin 2\pi(\phi_{67} - \phi_0)$, where $A = 5.6 \pm 0.2$, $B = 4.0 \pm 0.3$, and $\phi_0 = 0.76 \pm 0.1$ (hence peaks at $\phi_{67} = 0.01 \pm 0.01 \approx 0$), whereas during the dip the flux varies as $f_{\text{C IV, in}} (10^{-12} \text{ erg cm}^{-2} \text{ s}^{-1}) = C + D \sin 2\pi(\phi_{67} - \phi_0)$, where $C = 3.9 \pm 0.2$, $D = 1.6 \pm 0.2$, and $\phi_0 = 0.76 \pm 0.04$ (hence peaks at $\phi_{67} = 0.01 \pm 0.04 \approx 0$). The spin-phase variation of the C IV continuum flux density (specially, the model flux density at $\lambda = 1549.48$ Å) is shown in Figure 9. At least away from the dip, there is a tendency for the continuum flux density to be higher near $\phi_{67} = 0$ and lower near $\phi_{67} = 0.5$, but there is considerable scatter in the data at any spin phase.

The C IV line widths and radial velocities also follow from this parameterization of the spectra, although indirectly: the radial velocity is $v = c(\lambda_1 - \lambda_2)/\lambda_0$ and the line width (strictly, the separation of the two Gaussians) is $w = c(\lambda_1 + \lambda_2)/\lambda_0$. The most obvious variation is that of

w , which varies with spin phase as $w (10^3 \text{ km s}^{-1}) = \gamma + K \sin 2\pi(\phi_{67} - \phi_0)$, with $\gamma = 1.9 \pm 0.03$, $K = 0.34 \pm 0.04$, and $\phi_0 = 0.20 \pm 0.02$ (hence peaks at $\phi_{67} = 0.45 \pm 0.02 \sim 0.5$), but this variation is caused by the model’s fitting of the single-peaked line profiles (i.e., small Gaussian separations) during spin maximum and the double-peaked line profiles (i.e., large Gaussian separations) during spin minimum and does not translate into a variation in the net width of the line: the FWZI of the line is instead reasonably constant (with only a few exceptions, within 10%) at 30 Å or 5700 km s^{−1}. Like the C III λ1176 line (but unlike the O VI line) in the *ORFEUS* spectra, there is no radial velocity variation of the C IV line apparent on the white dwarf spin phase. However, as seen already in Figure 7, there is a tendency for the line to shift toward the blue during the dip (although the scatter in the individual measurements is large and the velocity difference is formally consistent with zero [$v = -680 \pm 710 \text{ km s}^{-1}$ during the dip compared to $v = 180 \pm 1600 \text{ km s}^{-1}$ away from the dip, where the errors are the square root of the sample variance relative to the weighted mean]). If the C IV radial velocity were as large as that of the O VI broad component, its amplitude would be roughly 1.7 Å, which is comparable to the width of the wavelength bins in the *IUE* spectra. Evidently, the complexity of the C IV line combined with the low spectral resolution and modest signal-to-noise ratio of the *IUE* spectra preclude centroiding the line to determine, or place useful limits on, its radial velocity.

5. Discussion

Before wading into details, it is useful to compare the mean *ORFEUS* spectrum of EX Hya with that of AM Her assembled from the six spectra obtained days earlier with the same instrument (Mauche & Raymond 1998, hereafter MR98). These mean FUV spectra are shown in Figure 10, where the spectrum of AM Her has been multiplied by $(75/100)^2$ to account for the relative distance to the two sources. Given that EX Hya (an IP with a truncated accretion disk) and AM Her (a polar without a disk) are physically such different sources, it is amazing that their FUV spectra are so similar. First, the *level* of the FUV continua are nearly identical. Second, the *shapes* of the FUV continua are nearly indistinguishable, even so far as (1) the absence of Lyman absorption lines and (2) the presence of the broad weak bump between the O VI and C III λ1176 emission lines. Third, both sources have C III, N III, and O VI emission lines with comparable widths and intensities; indeed, the intrinsic flux in the C III λ977 and N III λ991 emission lines are nearly identical. Fourth, both sources show broad and narrow component structure in the O VI emission line. With the exception of the absence of the He II λ1085 emission line in the spectrum of EX Hya, the *differences* between these spectra are in the details. First, the broad (narrow) component of the O VI line of EX Hya is stronger (weaker) than that of AM Her. Second, the C III λ1176 emission line of EX Hya is brighter and broader than that of AM Her.

Next consider the constraints imposed on the location of the continuum and emission-line regions by the phase-resolved *ORFEUS* spectra. First consider the broad-line region. MR98 identified the accretion funnel as the source of the broad component of the O VI emission line

in their *ORFEUS* spectra of AM Her. Consistent with simple expectations, in AM Her spin maximum of the FUV continuum and X-ray light curves occurs when the upper pole points *toward* the observer—when the *redshift* of the O VI broad component is the highest. Similarly, we identify the accretion funnel as the source of the O VI broad emission component in our *ORFEUS* spectra of EX Hya, but, consistent with the accretion curtain model, spin maximum of the FUV continuum and X-ray light curves occurs when the upper pole points *away* the observer—when the *blueshift* of the O VI broad component is the highest. This geometry implicates the accretion funnel itself as the source of the FUV continuum flux, not a separate intermediate-temperature spot on the surface of the white dwarf. If this is the case for both sources, it solves the problem of the absence of Lyman absorption lines in their FUV spectra. Next consider the narrow-line region. MR98 identified the irradiated face of the secondary as the source of the narrow component of the O VI emission line in their *ORFEUS* spectra of AM Her. The secondary cannot be the site of the narrow-line region in EX Hya, however, because maximum blueshift of the O VI narrow emission component occurs when the *white dwarf*, not the *secondary*, is moving toward the observer. Indeed, the radial velocity solution of the O VI narrow emission component ($K = 85 \pm 9 \text{ km s}^{-1}$, $\phi_0 = 0.54 \pm 0.02$; Table 3) is consistent with that of the Balmer line wings in the optical ($K = 69 \pm 9 \text{ km s}^{-1}$, $\phi_0 = 0.53 \pm 0.03$; Hellier et al. 1987), so we identify the white dwarf itself as the source of the O VI narrow emission component. With a FWHM $\approx 200 \text{ km s}^{-1}$, the O VI narrow emission component may ultimately prove to be better than the Balmer lines (for which FWHM $\sim 2000 \text{ km s}^{-1}$) for determining the radial velocity of the white dwarf in EX Hya.

Delving further into details, it is possible to combine information from the *ORFEUS* and *IUE* spectra of EX Hya to constrain the physical condition of the FUV and UV line-emitting plasma. First consider the broad-line region. In dense gas illuminated by hard X-rays (model 4 of Kallman & McCray 1982), O VI exists over a range of ionization parameters $\xi \equiv L/nr^2 \approx 40\text{--}70$ and temperatures $T \approx 40\text{--}130 \text{ kK}$. With $L \approx 2 \times 10^{32} \text{ erg s}^{-1}$ (Allan, Hellier, & Beardmore 1998), $n \gtrsim 2 \times 10^{11} \text{ cm}^{-3}$ for $r \leq 5 \times 10^9 \text{ cm} \approx 5 R_{\text{wd}}$. For the inferred range of ionization parameters, the dominant ionization stages of He, C, N, and Si are He II–III, C VI–VII, N VI–VII, and Si VI–XI, respectively, so if the observed lower ionization species dominate they must be produced in gas which is denser and/or lies further from the source of the ionizing flux. The observed line ratios may be affected by finite optical depths in the resonance lines, but modulo this effect the mean C III $\lambda 977/\lambda 1176$ line ratio of ~ 1.4 requires $n \gtrsim 10^{11} \text{ cm}^{-3}$ and $T \gtrsim 80 \text{ kK}$ (Keenan et al. 1992; Keenan 1997) and the mean Si III $\lambda 1300/\lambda 1890$ line ratio of $\gtrsim 10$ requires $n \gtrsim 10^{12} \text{ cm}^{-3}$ and $T \gtrsim 60 \text{ kK}$ (Nussbaumer 1986). The He II $\lambda 1085/\lambda 1640$ line ratio presents a puzzle. During spin maximum, the strength of the $\lambda 1640$ line in the *IUE* spectra is $f_{1640} \approx 1.5 \times 10^{-12} \text{ erg cm}^{-2} \text{ s}^{-1}$ (consistent with the *HUT* measurement), and the strength of the $\lambda 1085$ line in the *ORFEUS* spectra is $f_{1085} \lesssim 0.2 \times 10^{-12} \text{ erg cm}^{-2} \text{ s}^{-1}$ (a factor of $\gtrsim 2$ less than the uncertain *HUT* estimate), so the He II $\lambda 1085/\lambda 1640$ line ratio is $\lesssim 0.13$. For case B recombination, this ratio is > 0.13 for the full range of densities ($n = 10^2\text{--}10^{14} \text{ cm}^{-3}$) and temperatures ($T = 10\text{--}100 \text{ kK}$) tabulated by Storey & Hummer (1995), and is > 0.17 for $n > 10^{10} \text{ cm}^{-3}$ and $T < 100 \text{ kK}$. Variability could explain this discrepancy, but if it does not we must appeal to some process which preferentially

destroys $\lambda 1085$ line photons and/or enhances $\lambda 1640$ line photons. If the population of the $n = 2$ level is high enough to render the $\lambda 1085$ transition optically thick, there is a branching ratio of order one half to convert $\lambda 1085$ photons into a combination of He II Balmer ($\lambda 1216$, $\lambda 1640$), Paschen ($\lambda 4686$), and Brackett photons; this process would roughly double the flux of $\lambda 1640$ photons and thereby resolve the discrepancy. Simultaneously, it is possible for the He II Balmer β transition to be pumped by H I Lyman α photons, which generates $\lambda 1640$ and $\lambda 4686$ line photons when the ion decays. The strength of the $\lambda 4686$ line in the phase-averaged optical spectrum of Hellier et al. (1987) is uncertain because the absolute flux calibration is uncertain, but the measured value is $f_{4686} \sim 0.2 \times 10^{-12} \text{ erg cm}^{-2} \text{ s}^{-1}$, so the He II $\lambda 4686/\lambda 1640$ line ratio is ~ 0.13 . This ratio is consistent with the case B line ratios of Storey & Hummer, but it is unfortunately not diagnostic, given the uncertain calibration of the optical spectrum. Nonetheless, the available evidence points to the $\lambda 1085$ line flux being lower than expected, but since there are many ways for this to come about, in the absence of a detailed model it does not constrain the plasma conditions.

Next consider the narrow-line region, or more specifically why the irradiated face of the secondary of AM Her produces a narrow O VI emission line, while that of EX Hya does not. Shielding of the secondary by the accretion disk may play a role, but we argue that the fundamental reason is that the ionization parameter is simply too low. Although the luminosity of the hard component of the X-ray spectra of both AM Her and EX Hya is $L \approx 2 \times 10^{32} \text{ erg s}^{-1}$ (Ishida et al. 1997; Allan, Hellier, & Beardmore 1998), AM Her also has a soft component in its X-ray spectrum with $L \approx 2 \times 10^{33} \text{ erg s}^{-1}$ (Paerels et al. 1996). The ten times lower net ionizing luminosity of EX Hya is exacerbated by the lower efficiency of photoionization by hard X-rays, but is ameliorated by the factor of two smaller distance from the white dwarf to the face of the secondary. Specifically, whereas the ionization parameter of the irradiated face of the secondary of AM Her is $\xi \approx 2 \times 10^{33} \text{ erg s}^{-1} / 2 \times 10^{10} \text{ cm}^{-3} / (5.3 \times 10^{10} \text{ cm})^2 = 36$, for which O VI dominates for dense gas illuminated by a mixture of hard and soft X-rays (model 5 of Kallman & McCray 1982), that of EX Hya is $\xi \approx 2 \times 10^{32} \text{ erg s}^{-1} / 2 \times 10^{10} \text{ cm}^{-3} / (2.7 \times 10^{10} \text{ cm})^2 = 14$, for which O I dominates for dense gas illuminated by hard X-rays alone (model 4 of Kallman & McCray 1982). For O VI to dominate in EX Hya, the plasma must lie closer to the source of the ionizing flux. To satisfy the phasing of the radial velocity of the O VI narrow emission component, the narrow-line region must be closer to the white dwarf than the center of mass of the binary ($r < 6.7 \times 10^9 \text{ cm}$), hence $n \gtrsim 10^{11} \text{ cm}^{-3}$, consistent with the density derived above for the broad-line region. Based on the ratio R of the O VI line intensities shown in Table 2, the narrow-line region is optically thick ($R = 0.92 \pm 0.29$), while the broad-line region is more likely optically thin ($R = 1.8 \pm 1.0$).

6. Summary

Using *EUVE* photometry and *ORFEUS* and *IUE* spectroscopy, we have presented a detailed picture of the behavior of EX Hya in the vacuum ultraviolet. Consistent with its behavior in the optical, and hence consistent with the accretion curtain model of EX Hya, we find that the FUV

and UV continuum flux densities, the FUV and UV broad emission line fluxes, and the radial velocity of the O VI broad emission component all vary on the spin phase of the white dwarf, with the maximum of the FUV and UV continuum and broad emission line flux light curves coincident with maximum *blueshift* of the broad O VI emission component. On the binary phase, we find that the strong eclipse of the EUV flux by the bulge on the edge of the accretion disk is accompanied by narrow and relatively weak absorption components of the FUV emission lines and 30%–40% eclipses of all the UV emission lines except He II $\lambda 1640$, while the UV continuum is largely unaffected. Furthermore, both the flux and radial velocity of the O VI narrow emission component vary with binary phase. From the relative phasing of the FUV and UV continuum light curves and the FUV emission-line radial velocities, we identify the accretion funnel as the source of the FUV and UV continuum and the O VI broad emission component, and the white dwarf as the source of the O VI narrow emission component. The irradiated face of the secondary of EX Hya does not produce the narrow O VI emission component observed in *ORFEUS* spectra of AM Her because the ionization parameter (the X-ray luminosity) is too low. Various lines of evidence imply that the density of both the broad- and narrow-line regions is $n \gtrsim 10^{11} \text{ cm}^{-3}$, but the O VI line ratios imply that the narrow-line region is optically thick while the broad-line region is more likely optically thin. As in AM Her, it is likely that the velocity shear in the broad-line region allows O VI photons to escape, rendering the gas effectively optically thin.

We thank all those involved with making the *ORFEUS-SPAS II* mission a success: the members of the satellite and instrument teams at Institute for Astronomy and Astrophysics, University of Tübingen; Space Science Laboratory, University of California, Berkeley; and Landessternwarte Heidelberg-Königstuhl; the flight operations team; and the crew of STS-80. Special thanks (and apologies) are due to K. Mukai for acquiring the extensive set of *IUE* spectra used herein. F. Keenan is warmly thanked for supplying C III level population and line intensity data. Conversations and correspondence with B. Greeley, C. Hellier, K. Long, J. Raymond, and M. Sirk are gratefully acknowledged. This work was performed under the auspices of the U.S. Department of Energy by Lawrence Livermore National Laboratory under contract No. W-7405-Eng-48.

TABLE 1
Journal of *ORFEUS* Observations

Start Date (HJD – 2450000)	Exposure (s)	ϕ_{98}	ϕ_{67}
419.37867	1717	0.497– 0.788	0.341– 0.767
419.56674	2018	3.253– 3.595	4.381– 4.882
419.68857	2328	5.038– 5.433	6.998– 7.577
419.75218	1342	5.971– 6.208	8.365– 8.713
421.02764	1549	24.663–24.926	35.767–36.152

TABLE 3
Radial Velocities

Line	Component	γ (km s ⁻¹)	K (km s ⁻¹)	ϕ_0
O VI $\lambda\lambda$ 1032, 1038	N ^a	+45 \pm 6	85 \pm 9	0.54 \pm 0.02
O VI $\lambda\lambda$ 1032, 1038	B ^b	-79 \pm 59	332 \pm 65	0.30 \pm 0.07
C III λ 1176	B ^a	-40 \pm 40	118 \pm 56	0.39 \pm 0.08
C III λ 1176	B ^b	-40 \pm 39	113 \pm 47	0.51 \pm 0.08

$$^a v = \gamma + K \sin 2\pi(\phi_{98} - \phi_0).$$

$$^b v = \gamma + K \sin 2\pi(\phi_{67} - \phi_0).$$

TABLE 4
Journal of *IUE* Observations^a

Sequence Number	Start Date (HJD – 2440000)	ϕ_{98}	ϕ_{67}
SWP 17598	5187.15547	0.736– 0.889	0.999– 0.223
SWP 23199	5859.18716	0.685– 0.889	0.937– 0.235
SWP 26547	6282.38720	0.887– 0.009	0.976– 0.155
SWP 28858	6649.95322	0.744– 0.151	0.775– 0.372
SWP 47643	9118.84774	0.587– 0.009	0.630– 0.249
SWP 55063	9892.07765	0.645– 0.747	0.760– 0.909
SWP 55064	9892.10641	1.067– 1.168	1.378– 1.527
SWP 55065	9892.13367	1.466– 1.568	1.964– 2.113
SWP 55066	9892.16015	1.854– 1.956	2.532– 2.681
SWP 55067	9892.18676	2.244– 2.346	3.104– 3.253
SWP 55068	9892.21373	2.639– 2.741	3.683– 3.832
SWP 55069	9892.23968	3.020– 3.121	4.241– 4.390
SWP 55070	9892.27026	3.468– 3.570	4.898– 5.047
SWP 55071	9892.29733	3.865– 3.966	5.480– 5.629
SWP 55073	9892.35149	4.658– 4.760	6.643– 6.792
SWP 55074	9892.39783	5.338– 5.439	7.639– 7.788
SWP 55075	9892.42914	5.796– 5.898	8.311– 8.460
SWP 55076	9892.46114	6.265– 6.367	8.999– 9.148
SWP 55077	9892.49171	6.713– 6.815	9.656– 9.805
SWP 55078	9892.52777	7.242– 7.344	10.430–10.579
SWP 55079	9892.55893	7.699– 7.800	11.100–11.249
SWP 55080	9892.59520	8.230– 8.332	11.879–12.028
SWP 55081	9892.62656	8.690– 8.791	12.553–12.702

SWP 55082	9892.65456	9.100– 9.202	13.154–13.303
SWP 55083	9892.68347	9.524– 9.625	13.775–13.924
SWP 55084	9892.71699	10.015–10.117	14.495–14.644
SWP 55086	9892.77016	10.794–10.896	15.638–15.787
SWP 55087	9892.79685	11.185–11.287	16.211–16.360
SWP 55088	9892.82308	11.570–11.671	16.775–16.924
SWP 55089	9892.84972	11.960–12.062	17.347–17.496
SWP 55091	9892.90274	12.737–12.839	18.486–18.635
SWP 55092	9892.93000	13.137–13.238	19.072–19.221
SWP 55093	9892.95751	13.540–13.642	19.663–19.812
SWP 55094	9892.98448	13.935–14.037	20.242–20.391
SWP 55095	9893.01235	14.344–14.445	20.841–20.990
SWP 55097	9893.06511	15.117–15.219	21.974–22.124
SWP 55098	9893.09177	15.508–15.609	22.547–22.696
SWP 55099	9893.12323	15.969–16.070	23.223–23.372
SWP 55100	9893.15120	16.379–16.480	23.824–23.973
SWP 55101	9893.17884	16.784–16.885	24.418–24.567
SWP 55102	9893.20700	17.196–17.298	25.023–25.172
SWP 55103	9893.23465	17.602–17.703	25.617–25.766
SWP 55104	9893.26278	18.014–18.116	26.221–26.370
SWP 55105	9893.28999	18.413–18.514	26.806–26.955
SWP 55106	9893.31825	18.827–18.928	27.413–27.562
SWP 55107	9893.35007	19.293–19.395	28.097–28.246

^aExposures are as follows. SWP 17598: 900 s, SWP 23199: 1200 s, SWP 26547: 721 s, SWP 28858: 2400 s, SWP 47643: 2489 s, SWP 55063–55107: 600 s.

REFERENCES

- Allan, A., Hellier, C., & Beardmore, A. 1998, MNRAS, 295, 167
- Bath, G. T., Pringle, J. E., & Whelan, J. A. J. 1980, MNRAS, 190, 185
- Beuermann, K., & Osborne, J. P. 1988, A&A, 189, 128
- Buckley, D. A. H., & Warner, B. 1995, Cape Workshop on Magnetic Cataclysmic Binaries (San Francisco: ASP)
- Cropper, M. 1990, Space Sci. Rev., 54, 195
- Fujimoto, R., & Ishida, M. 1997, ApJ, 474, 774
- Greeley, B. W., Blair, W. P., Long, K. S., & Knigge, C. 1997, ApJ, 488, 419
- Hellier, C. 1996, in Cataclysmic Variables and Related Objects, ed. A. Evans & J. H. Wood (Dordrecht: Kluwer), 143
- Hellier, C., Mason, K. O., Rosen, S. R., & Córdoba, F. A. 1987, MNRAS, 228, 463
- Hellier, C., & Mukai, K. 1999, Proceedings of the Annapolis Workshop on Magnetic Cataclysmic Variables, (San Francisco: ASP)
- Hellier, C., & Sproats, L. N. 1992, IBVS, 3724
- Hurwitz, M., et al. 1998, ApJ, 500, L1
- Hurwitz, M., & Bowyer, S. 1986, Proc. SPIE, 627, 375
- Hurwitz, M., & Bowyer, S. 1996, in Astrophysics in the Extreme Ultraviolet, ed. S. Bowyer & R. F. Malina (Dordrecht: Kluwer), 601
- Hurwitz, M., Sirk, M., Bowyer, S., & Ko, Y.-K. 1997, ApJ, 477, 390
- Ishida, M., Matsuzaki, K., Fujimoto, R., Mukai, K., & Osborne, J. P. 1997, MNRAS, 287, 651
- Kallman, T. R., & McCray, R. 1982, ApJS, 50, 263
- Keenan, F. P., Feibelman, W. A., & Berrington, K. A. 1992, ApJ, 389, 443
- Keenan, F. P. 1997, personal communication
- Krautter, J., & Buchholz, W. 1990, in Accretion-Powered Compact Binaries, ed. C. W. Mauche (Cambridge: CUP), 229
- la Dous, C. 1991, A&A, 252, 100
- Mattei, J. A. 1998, Observations from the AAVSO International Database, personal communication

- Mauche, C. W., Lee, Y. P., & Kallman, T. R. 1997, *ApJ*, 477, 832
- Mauche, C. W., & Raymond, J. C. 1998, *ApJ*, 505, 869, MR98
- Mukai, K., Ishida, M., Osborne, J., Rosen, S., & Stavroyiannopoulos, D. 1998, in *Wild Stars in the Old West*, ed. S. Howell, E. Kuulkers, & C. Woodward (San Francisco: ASP), 554
- Nussbaumer, H. 1986, *A&A*, 155, 205
- Paerels, F., Hur, M. H., Mauche, C. W., & Heise, J. 1996, *ApJ*, 464, 884
- Patterson, J. 1994, *PASP*, 106, 209
- Rosen, S. R., Mason, K. O., & Córdova, F. A. 1988, *MNRAS*, 231, 549
- Rosen, S. R., Mason, K. O., Mukai, K., & Williams, O. R. 1991, *MNRAS*, 249, 417
- Siegel, N., Reinsch, K., Beuermann, K., van der Woerd, H., & Wolff, E. 1989, *A&A*, 225, 97
- Storey, P. J., & Hummer, D. G. 1995, *MNRAS*, 272, 41
- Verbunt, F. 1987, *A&AS*, 71, 339
- Warner, B. 1995, *Cataclysmic Variable Stars* (Cambridge: Cambridge University Press)

Fig. 1.— Spin- (*upper panel*) and binary-phase (*middle and lower panels*) *EUVE* deep survey light curves of EX Hya. One hundred phase bins are used in the upper two panels and 589 (10 second bins) are used in the lower panel. In the upper two panels a typical error bar (± 0.012 counts s^{-1}) is indicated by the cross. The numbered horizontal lines indicate the relative phases of the *ORFEUS* spectra. For reference, $0.2 \text{ counts s}^{-1} \approx 2 \times 10^{-11} \text{ erg cm}^{-2} \text{ s}^{-1}$.

Fig. 2.— *ORFEUS* spectra of EX Hya ordered by white dwarf spin phase. Each successive spectrum is offset by 0.75 flux density units. Two-component (20 + 37 kK) blackbody models are shown by the light-colored nearly straight curves.

Fig. 3.— Mean flux density at $\lambda = 1010 \pm 5 \text{ \AA}$ in units of $10^{-12} \text{ erg cm}^{-2} \text{ s}^{-1} \text{ \AA}^{-1}$ as a function of white dwarf spin phase.

Fig. 4.— Regions of the *ORFEUS* spectra containing the O VI doublet showing Gaussian fits to the broad and narrow components. Panels are ordered by relative white dwarf spin phase.

Fig. 5.— *Upper panel*: Radial velocity of the broad component of the O VI doublet as a function of white dwarf spin phase. *Lower panel*: Radial velocity of the narrow component of the O VI doublet as a function of binary phase.

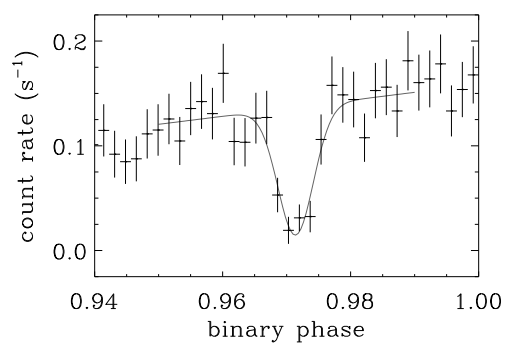
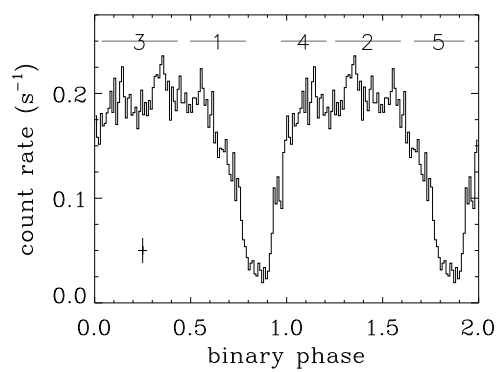
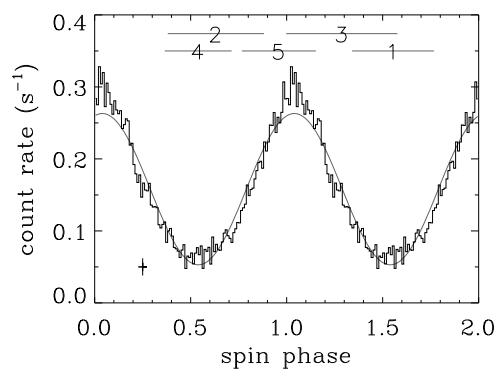
Fig. 6.— *Upper panel*: Flux of the broad component of the O VI doublet as a function of white dwarf spin phase. *Lower panel*: Flux of the narrow component of the O VI doublet as a function of binary phase.

Fig. 7.— Mean phase-resolved *IUE* spectra of EX Hya for the following spin/binary phases: (a) maximum/non-dip, (b) maximum/dip, (c) minimum/dip, and (d) minimum/non-dip. Reseaux are marked by crosses (\times).

Fig. 8.— Flux of the C IV doublet as a function of white dwarf spin phase away (*upper panel*) and during (*lower panel*) the dip in the orbital light curve.

Fig. 9.— Flux density at $\lambda = 1549.48 \text{ \AA}$ as a function of white dwarf spin phase away (*upper panel*) and during (*lower panel*) the dip in the orbital light curve.

Fig. 10.— Mean *ORFEUS* spectra of EX Hya (*thick histogram*) and AM Her [multiplied by $(75/100)^2$ to account for the relative distance to the two sources] (*light-colored histogram*).



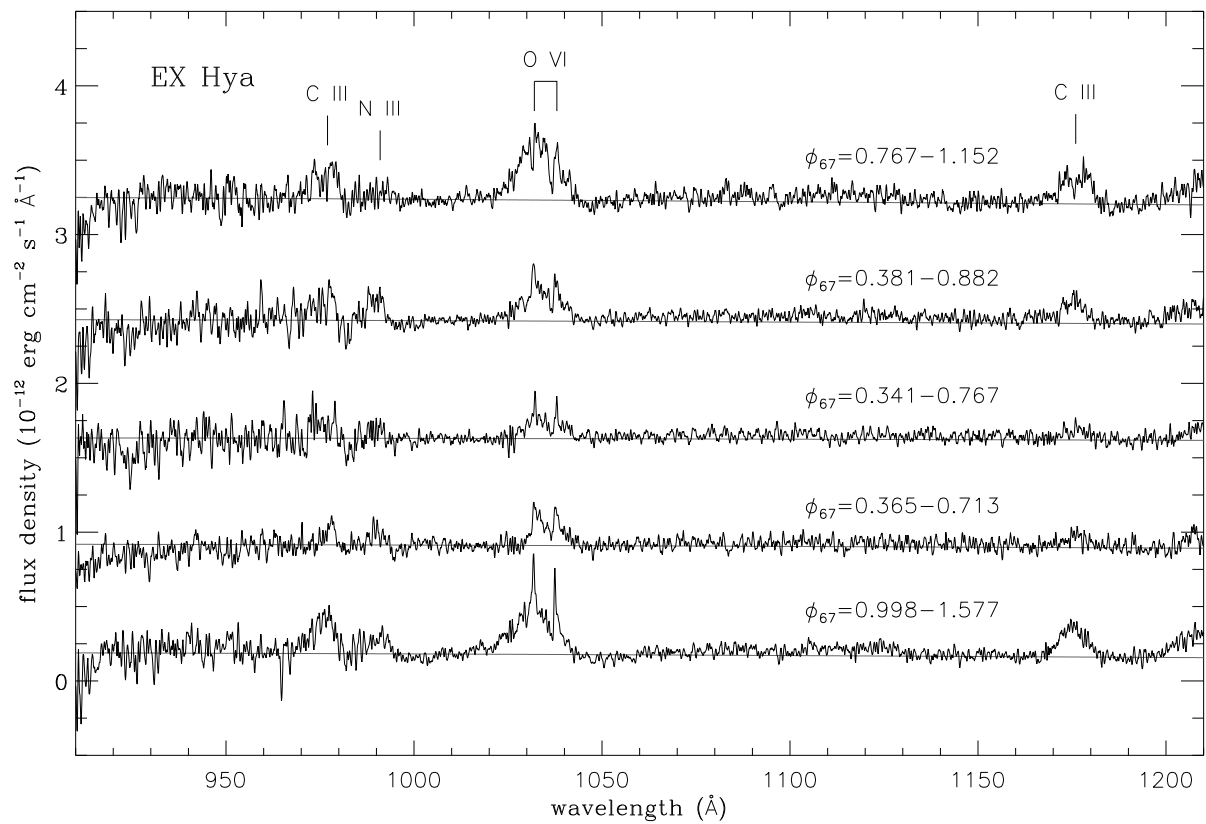


TABLE 2
O VI Line Parameters

ϕ_{67}	Narrow Component				Broad Component		
	$f(1032 \text{ \AA})$ ($10^{-12} \text{ erg cm}^{-2} \text{ s}^{-1}$)	$f(1038 \text{ \AA})$ ($10^{-12} \text{ erg cm}^{-2} \text{ s}^{-1}$)	Velocity (km s^{-1})	FWHM ^a (km s^{-1})	$f(1032 \text{ \AA})$ ($10^{-12} \text{ erg cm}^{-2} \text{ s}^{-1}$)	$f(1038 \text{ \AA})$ ($10^{-12} \text{ erg cm}^{-2} \text{ s}^{-1}$)	Velocity (km s^{-1})
0.998–1.577	0.23 ± 0.04	0.23 ± 0.03	-36 ± 5	134 ± 12	2.7 ± 0.4	0.7 ± 0.5	-190 ± 10
0.365–0.713	0.14 ± 0.05	0.18 ± 0.06	$+25 \pm 22$	272 ± 58	0.9 ± 0.1	0.6 ± 0.1	$+381 \pm 10$
0.341–0.767	0.10 ± 0.02	0.09 ± 0.02	$+89 \pm 7$	105 ± 16	0.8 ± 0.1	0.4 ± 0.1	$+43 \pm 10$
0.381–0.882	0.22 ± 0.05	0.16 ± 0.04	$+8 \pm 17$	290 ± 41	1.5 ± 0.3	0.7 ± 0.4	$+115 \pm 10$
0.767–1.152	0.14 ± 0.05	0.21 ± 0.06	$+158 \pm 23$	279 ± 54	3.3 ± 0.3	1.5 ± 0.3	-346 ± 10

^aInstrumental profile FWHM $\approx 95 \text{ km s}^{-1}$.

